

# Geophysical Research Letters

## RESEARCH LETTER

10.1029/2020GL088867

### Key Points:

- Discrete collapse events exhibit radial outward displacements up to 20 cm and uplift of over 5 cm outside caldera
- Data best fit by slip on normal ring fault that steepens with depth and associated pressurization of underlying magma chamber
- Triaxial point source fits the data well but yields a strongly biased estimate of the source depth and kinematics

### Supporting Information:

- Supporting Information S1

### Correspondence to:

P. Segall,  
segall@stanford.edu

### Citation:

Segall, P., Anderson, K. R., Pulvirenti, F., Wang, T., & Johanson, I. (2020). Caldera collapse geometry revealed by near-field GPS displacements at Kilauea Volcano in 2018. *Geophysical Research Letters*, 47, e2020GL088867. <https://doi.org/10.1029/2020GL088867>

Received 15 MAY 2020

Accepted 12 JUL 2020

Accepted article online 17 JUL 2020

## Caldera Collapse Geometry Revealed by Near-Field GPS Displacements at Kilauea Volcano in 2018

Paul Segall<sup>1</sup> , Kyle R. Anderson<sup>2</sup> , Fabio Pulvirenti<sup>3</sup> , Taiyi Wang<sup>1</sup>, and Ingrid Johanson<sup>4</sup> 

<sup>1</sup>Geophysics, Stanford University, Stanford, CA, USA, <sup>2</sup>California Volcano Observatory, U.S. Geological Survey, Moffet Field, CA, USA, <sup>3</sup>Jet Propulsion Laboratory, California Institute of Technology, Pasadena, CA, USA, <sup>4</sup>Hawaiian Volcano Observatory, U.S. Geological Survey, Hilo, HI, USA

**Abstract** We employ near-field GPS data to determine the subsurface geometry of a collapsing caldera during the 2018 Kilauea eruption. Collapse occurred in 62 discrete events, with “inflationary” deformation external to the collapse, similar to previous basaltic collapses. We take advantage of GPS data from the collapsing block and independent constraints on the magma chamber geometry from inversion of deflation prior to collapse onset. This provides an unparalleled opportunity to constrain the collapse geometry. Employing an axisymmetric finite element model, the co-collapse displacements are best explained by piston-like subsidence along a high angle ( $\sim 85^\circ$ ) normal ring fault that may steepen to vertical with depth. Reservoir magma has compressibility of  $2\text{--}15 \times 10^{-10} \text{ Pa}^{-1}$ , indicating bubble volume fractions from 1% to 7% (lower if fault steepens with depth). Magma pressure increases during collapses are 1 to 3 MPa, depending on compressibility. Depressurization of a triaxial point source in a homogeneous half-space fits the data well but provides a biased representation of the source depth and process.

**Plain Language Summary** When large volumes of magma erupt rapidly, the rock overlying the subsurface reservoir founders, producing a caldera. During the 2018 eruption of Kilauea Volcano, Hawai‘i, collapse occurred in over 60 events, each lasting 5 to 10 s. We analyze GPS data collected during the last 32 of these events to determine the geometry of the ring fault system bounding the caldera block and the properties of the underlying magma. The faults are on average very steep but dip slightly inward at shallow depth. Inferred pressure increases during collapse events constrain the compressibility of the magma and imply an exsolved gas phase with 1% to 7 % bubbles by volume.

## 1. Introduction

The largest volcanic eruptions are accompanied by caldera collapse (Branney & Acocella, 2015). While caldera formation is understood to result from the rapid withdrawal of large volumes of magmas from crustal reservoirs, the geometry of these reservoirs and in particular the dip of the ring fault systems (normal vs. reverse) are not well understood. Constraints come from geologic observations of eroded calderas, geophysical observations, and analog and numerical modeling (Branney & Acocella, 2015; Cole et al., 2005). Caldera collapses are thankfully rare, and relatively little data have been collected in the near field of an ongoing collapse.

Historic caldera collapses at basaltic shield volcanoes occur in discrete events (Gudmundsson et al., 2016; Kumagai et al., 2001; Michon et al., 2009); the Kilauea 2018 eruption consisted of 62 such collapse events (Neal et al., 2019; Tepp et al., 2020). These events were accompanied by very long period (VLP) earthquakes and remarkable “inflationary” deformation (Figure 1). Similar behavior was observed at Miyakejima, Japan, and Piton de la Fournaise on Reunion Island (Kumagai et al., 2001; Michon et al., 2009). Kilauea high rate GPS data show that the collapse events took place over 5 to 10 s. During this time negligible magma could have left the underlying chamber, meaning that collapses occurred under constant mass conditions. Segall et al. (2019) showed that under these conditions co-collapse deformation results from a combination of chamber pressurization and fault slip. For a vertical ring fault the deformation external to the collapse is caused solely by pressure increase in the chamber; for other dips fault-induced deformation contributes to surface displacements and tilts.

The eruption of Kilauea in 2018 provided unique data during a caldera collapse (Anderson et al., 2019; Neal et al., 2019; Tepp et al., 2020). The eruption began on 3 May 2018 in the lower East Rift Zone (ERZ). Deflation

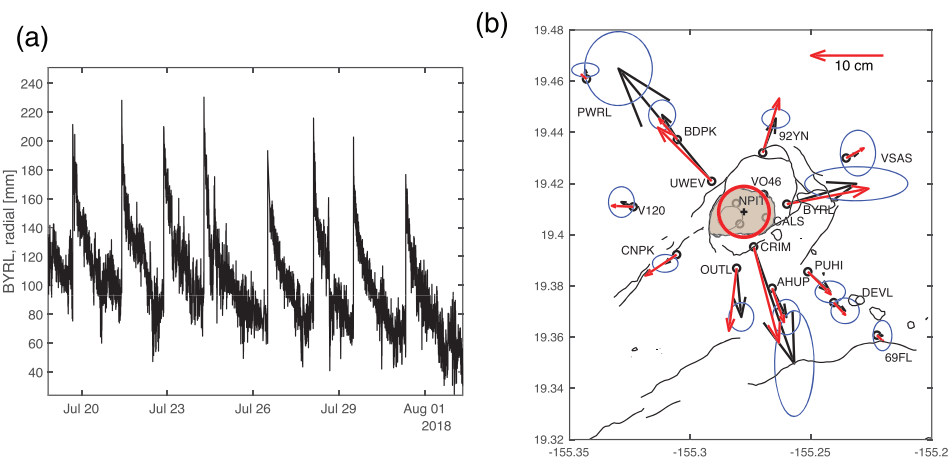


**Figure 1.** (a) Time series of radial component GPS displacements at BYRL. Positive displacement indicates motion away from the caldera. Station location shown in (b). (b) Co-collapse radial displacements. Black: average of last 32 collapse events, with 95% confidence ellipses reflecting the variability of the individual events. Red: predicted by model with fault dip increasing from  $85^\circ$  to vertical at 600 m (see Figure 2) and magma compressibility  $\beta_m = 3 \times 10^{-10} \text{ Pa}^{-1}$ . Collapse structure is shaded. Red circle shows location of model ring fault. Scale vector is 0.1 m.

at Kilauea's summit began the previous day and accelerated following a  $M 6.9$  south flank earthquake on 4 May. On 16 May the first rapid inflation event occurred contemporaneous with significant ash emission. By 29 May fault-bounded collapse was evident outside of Halema'uma'u crater. Later in the eruption collapse events were accompanied by higher effusion rates at the eruption site (Patrick et al., 2019). During June a new surface fault scarp propagated clockwise through the existing (1500 CE) Kilauea caldera, establishing a roughly circular collapse structure by middle to late June 2018. The floor of Halema'uma'u crater ultimately dropped up to 500 m, and the volume of the caldera increased by  $\sim 0.8 \text{ km}^3$ .

Here we build on the conceptual modeling of Segall et al. (2019); specifically, we use near-field GPS data to constrain collapse structure at depth. We develop a forward model conditioned on observations prior to collapse onset. Unknown parameters are constrained by near-field, co-collapse GPS displacements. To contrast with point source models commonly employed in volcano deformation studies, we compare results with inversions based on a triaxial point source in a homogeneous half-space. The point source has more degrees

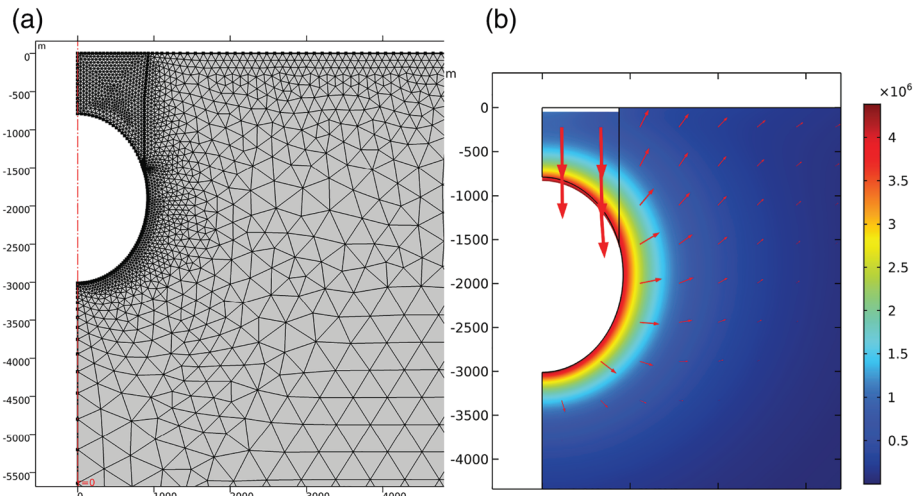


**Figure 2.** (a) A portion of the finite element mesh showing the magma chamber and an inward-dipping fault that steepens with depth. Geometry is radially symmetric about the red dashed line. (b) Maximum shear (von Mises) stress for vertical ring fault. Vectors represent displacements with log scaling to permit viewing of displacements outside the collapse piston. Note that stresses are due solely to chamber pressurization.

of freedom than the finite element method (FEM)-based model and is not restricted to radial symmetry. Nevertheless, it cannot capture the kinematics of the collapse and could lead to biased interpretations. Because the eruptive vents were separated from the caldera in 2018, we draw no conclusions here concerning relevance to silicic caldera collapse.

## 2. Method

We analyze high rate GPS data (5 s sampling) from collapse events later in the eruption, after the eastern section of the ring fault system was fully formed. A sample time series for Station BYRL is shown in Figure 1a. The co-collapse displacement in individual events was determined as the difference between preevent and postevent positions averaged over 4 min, not including a window  $\pm 30$  s around the time of the event. We then computed the mean and variance of the co-collapse displacements for the last 32 events. We find that stations closest to the collapse have more variability and are thus downweighted relative to more distant stations in our inversions. An alternate approach is to stack the time series at each station (last 32 events) and then compute co-collapse displacements from the stack. Uncertainties are computed by averaging the standard errors of the mean in the stacks and then differencing the mean in the precollapse and postcollapse windows and propagating these into the difference assuming they are uncorrelated. While these two approaches lead to essentially identical displacements, the second results in substantially smaller but more uniform uncertainties. For completeness we present results with both sets of weights.

We take advantage of constraints on the magma chamber geometry inferred from analysis of precollapse subsidence measured by GPS, tilt, and interferometric synthetic aperture radar (InSAR) (Anderson et al., 2019). We take the median values for the chamber parameters to construct a radially symmetric FEM model of a typical collapse event (Figure 2). The model consists of an ellipsoidal reservoir and a ring fault from the surface to the magma chamber. Of course, neither the collapse geometry nor displacements are radially symmetric (Figure 1b). Rather, the collapse occurred on preexisting faults along much of the south and west margins, whereas a new (at least at the surface) intracaldera fault developed along the east margin of the 2018 collapse. High-frequency (volcano tectonic, VT) seismicity was concentrated along this new structure (Shelly & Thelen, 2019).

From Anderson et al. (2019) (see supporting information, SI) the median magma chamber has initial volume  $V=3.9 \text{ km}^3$  and centroid depth 1.9 km, whose apex reaches to  $\sim 0.8$  km below the surface (Figure 2). Note that the precollapse model places only first-order constraints on the shape of and depth to the top of the reservoir. The average vertical displacement during the last 32 collapse events, from GPS Station CALS located on the downdropped block (Figure 1b) was  $\sim 2.5$  m. Thus, fault slip, assumed for simplicity to be uniform along the ring fault, is taken as  $2.5/\sin(\delta)$  m, where  $\delta$  is fault dip.

The surface deformation during collapse events depends on the geometry of the magma chamber and ring fault system, and the pressure change induced by reduction in chamber volume due to downward motion of the roof block. As shown in the SI, the co-collapse displacements  $u_{\text{co}}(\mathbf{x})$  at radial position  $\mathbf{x}$  are

$$u_{\text{co}}(\mathbf{x}) = s \left[ \frac{-\Phi(\mathbf{m}, \delta)f(\mathbf{x}; \mathbf{m})}{\mu(\beta_m + \beta_c)} + g(\mathbf{x}; \mathbf{m}, \delta) \right]. \quad (1)$$

Here  $s$  is fault slip,  $f(\mathbf{x}; \mathbf{m})$  is function of model parameters  $\mathbf{m}$  that characterize the chamber (depth to centroid, vertical and horizontal semiaxes);  $g(\mathbf{x}; \mathbf{m}, \delta)$  is a dimensionless function that maps slip to displacement at constant chamber pressure. Further,  $\Phi \equiv \partial V/\partial s$  at constant pressure,  $p$ . Finally,  $\mu$  is the crustal shear modulus, and  $\beta_m$  and  $\beta_c \equiv (1/V)\partial V/\partial p$  are the magma and chamber compressibilities. The latter depends on  $\mu$  and chamber geometry. Note that  $\Phi f$  and  $\mu(\beta_m + \beta_c)$  are dimensionless.

The average elastic properties of the crust are imperfectly known but are chosen to be consistent with the precollapse modeling. The surface expression of the ring fault is constrained by direct observation and roughly coincides with the inferred outline of the magma chamber (Anderson et al., 2019). By fixing the geometry (including  $V$ ) and  $\mu$ , which determines both  $\beta_c$  and  $\Phi$  to that estimated from precollapse data, the only unknown parameters are fault dip and magma compressibility. We search over  $(\delta, \beta_m)$  space to determine parameters that optimize fit to the co-collapse data.

Equation 1 is important for understanding how the data scale with mechanical and geometric parameters. As described in the SI, the pressure change in the first term does not appear explicitly. However, in the FEM calculations  $\Delta p_{\text{co}}$  induced by collapse is computed by

$$\Delta p_{\text{co}} = -\frac{\Delta V}{V\beta_m}, \quad (2)$$

where  $\Delta V$  is the change in chamber volume.

We use the finite element code COMSOL Multiphysics to determine the surface deformation due to fault slip on a ring fault coupled to a magma chamber (Figure 2). Slip is spatially uniform and imposed on the ring fault. Displacement of the plug into the chamber reduces its volume, increasing magma pressure according to Equation 2. This spatially uniform pressure change and zero shear traction provide the boundary condition on the walls of the chamber. The model domain dimensions are 20 times the largest dimension of the chamber, sufficient to avoid boundary effects; results are insensitive to further mesh refinement. The following section describes how we search over a range of fault dips and magma compressibilities and compare to the observed displacements.

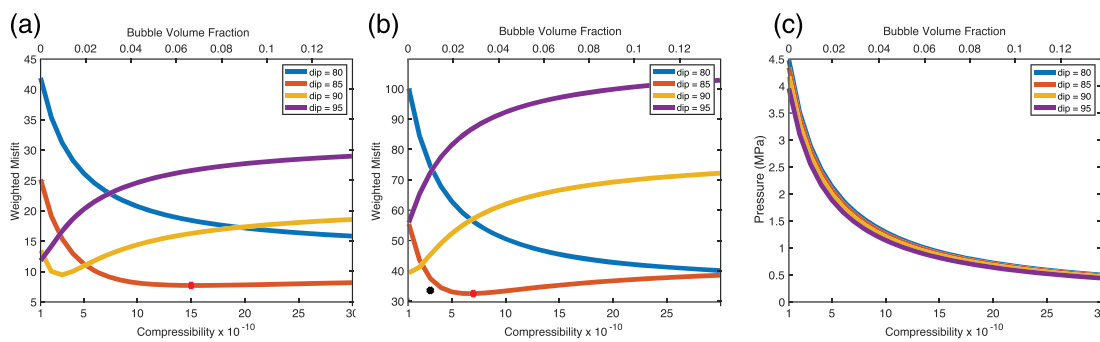
### 3. Results

Figure 3 shows misfit, defined as the weighted residual 2-norm, including vertical and radial displacements, as a function of dip (in 5° increments) and compressibility. Figure 3a shows results with weights determined by the variance of the events, while Figure 3b employs the lower variance determined from the stacked time series. In both cases a (normal) dip of 85° fits the data best over a range of compressibilities, with optimal values of  $\beta_m$  of 15 and  $7 \times 10^{-10} \text{ Pa}^{-1}$ , respectively. Vertical ring faults with  $\beta_m = 1 \rightarrow 3 \times 10^{-10} \text{ Pa}^{-1}$  also fit the data with larger errors reasonably well (Figure 3a). Shallower normal faults ( $\delta \leq 85^\circ$ ) and reverse faults ( $\delta=95^\circ$ ) generally do not fit the data well.

Figures 4a and 4b compare radial and vertical displacements as a function of distance from the collapse center with predictions from the FEM model for the optimal magma compressibility,  $\beta_m = 7 \times 10^{-10} \text{ Pa}^{-1}$  and a range of ring fault dips. The 85° dipping ring fault fits data quite well, although underpredicting the radial displacements of the nearest stations (CRIM and UWEV). As noted by Segall et al. (2019), outward dips ( $\delta > 90^\circ$ ) result in inward directed (negative) displacements close to the collapse, contrary to observations. This is most pronounced with compressible magmas because of the smaller pressure change (Figure 3c), which increases the relative contribution of the ring fault to the surface deformation. With less compressible magmas (see the SI) the predicted radial displacements are outward but decrease as the ring fault is approached, contrary to the data (SI Figure S1). These observations exclude an outward-dipping ring fault. With the compressibility of gas free basalt, the minimum reasonable value,  $\beta_m \sim 1 \times 10^{-10} \text{ Pa}^{-1}$ , the model overpredicts the vertical displacements for all dips (SI). As described in section 4, these results imply the presence of an exsolved vapor phase in the magma chamber.

Figures 4c and 4d illustrate results for  $\beta_m = 3 \times 10^{-10} \text{ Pa}^{-1}$ , near the local minimum in misfit for a vertical ring fault (Figure 3a). For this compressibility, the vertical ring fault fits the radial displacements well at more distant stations (Figure 4c) but significantly underpredicts the radial displacements at the closer stations. While the 85° dipping fault better fits the close-in radial displacements, it overpredicts both the more distant stations as well as the vertical displacements. This suggests that the ring fault may steepen with depth, which we tested for a number of scenarios. Figures 4c and 4d show the prediction for a ring fault that dips 85° at the surface and steepens to vertical at 600 m depth (Figure 2a). As expected, this fits the radial displacements at the more distant stations and does a better job of fitting the closer stations. It overpredicts the vertical displacements but generally fits the data within one standard deviation. Dips that steepen with depth are consistent with field observations that show inward (normal) dips at the surface. (The ratio of vertical to horizontal displacements at CALS [see Figure 1b] indicates a dip at the Earth's surface of 71.5°.)

The fit to the horizontal displacements of the steepening fault model is shown in Figure 1b. The model underpredicts the displacement at UWEV and overpredicts the displacements at CNPK and 92YN, a consequence of the assumed radial symmetry. Some aspect of the ring fault chamber system led to larger displacements in the northwestern direction at UWEV, although BDPK is fit well, suggesting that this feature is



**Figure 3.** Weighted residual norm as a function of fault dip and magma compressibility. Red dot indicates minimum misfit. Top axis gives the implied bubble volume fraction (see section 4). (a) Standard deviation determined from the 32 separate events. (b) Standard deviation determined from stack of events. Black dot indicates misfit for fault with dip that steepens from 85° to vertical at 600 m depth. (c) Computed pressure change in the magma chamber.

shallow. One possibility is a locally shallower dip along this section of the ring fault. It is also possible that there is some asymmetry in the shallow magma reservoir, although asymmetry in the pre-collapse deformation was small (Anderson et al., 2019). Given the symmetry of the forward model and the fact that only two parameters are adjusted, the fit is reasonable.

The pressure increase during a typical collapse event is shown in Figure 3c. Because the slip amplitude is specified, less compressible magmas result in larger pressure increases (Equation 2). Fault dip has a minor effect with normal faulting giving slightly larger pressure increases. Given the range of parameters that fit the data, our results suggest that pressure increases ranged from 3.3 MPa (for a vertical ring fault and a compressibility of  $2 \times 10^{-10}$  Pa<sup>-1</sup>) to 1.25 MPa (for an 85° dip and compressibility of  $10^{-9}$  Pa<sup>-1</sup>.)

#### 4. Discussion

The compressibility of gas-free basalt melt is  $\beta_l \sim 1 \times 10^{-10}$  Pa<sup>-1</sup> (Murase & McBirney, 1973; Spera, 2000). Our results suggest the compressibility of magma in the Halema‘uma‘u reservoir is  $\beta_m = 2 \rightarrow 15 \times 10^{-10}$  Pa<sup>-1</sup>, implying an exsolved gas phase. The magma compressibility can be expressed in terms of the volume fraction of gas phase  $\phi$ ,

$$\beta_m = (1 - \phi)\beta_l + \phi\beta_g = (1 - \phi)\beta_l + \phi/p, \quad (3)$$

where the gas is assumed to be ideal. Taking the pressure to be magmastic at the chamber centroid depth, with density  $2.5 \times 10^3$  kg/m<sup>3</sup> implies vesicularities of  $\phi$  of 0.01 to 0.07 and possibly as high as 0.12 (Figure 3). If the bubble fraction is vertically stratified, then the average compressibility would be a volume-weighted average over depth (similar to Equation 3). For example, if there was a thin bubble-rich layer near the top of the chamber, its compressibility, and hence bubble fraction, could be much larger than stated above. Given that bubbles rise rapidly in low viscosity basalt, high in situ gas volume fractions may be unrealistic; however, it is beyond our scope to bound plausible values. It also should be noted from Equation 1 that displacements depend on the product of shear modulus  $\mu$  and total compressibility. It is possible that the effective shear modulus for short-duration collapse events may have been greater than that for weeks-long deflation (e.g., Mavko et al., 2020). If so, this could be consistent with lower compressibility and vesicularity.

We used the ~2.5 m rapid downward displacement of CALS (Figure 1b) to measure sudden collapse in a typical event. CALS also experienced ~2 m slow subsidence between collapse events. This may reflect fault creep, perhaps localized along the newer, eastern sector of the ring fault associated with abundant VT seismicity (Shelly & Thelen, 2019). Because CALS is close to the eastern ring fault, it is possible that it is unrepresentative of the collapse as a whole. If the subsidence experienced by the bulk of the collapse was equal to the cumulative displacement at CALS, it would have been closer to 4.5 m.

The cumulative displacements recorded from repeated digital elevation models (DEMs) provide another estimate of the vertical drop in an average collapse. Between 13 July and the end of the eruption the eastern block subsided about 60–70 m, in 13 events, or ~5 m per event. However, this does not determine how much

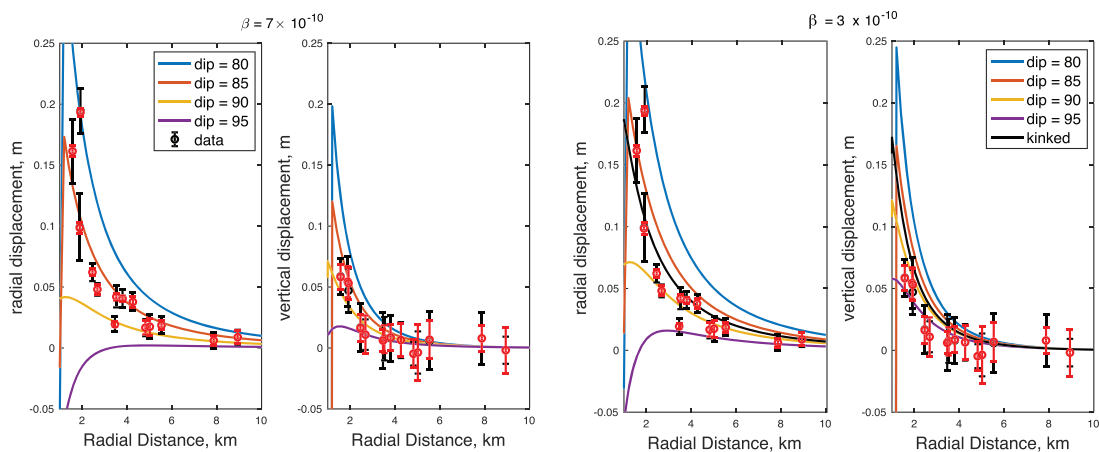


**Figure 4.** Predicted (lines) and observed (circles with error bars) radial (a, c) and vertical (b, d) displacements during a collapse event; 1-sigma error bars; simple averaging (black) and stacking (red). Predictions are shown for a range of dips (dips less than 90° are normal faults) and  $\beta_m = 7 \times 10^{-10} \text{ Pa}^{-1}$  (a, b) and for  $\beta_m = 3 \times 10^{-10} \text{ Pa}^{-1}$  (c, d). Also shown is the case with fault dip that steepens from 85° to vertical at a depth of 600 m, labeled “kinked.”

was slow interevent subsidence. We find that solutions with 5 m of slip do not fit as well, especially at the closest stations, and favor vertical ring faults. Because the slow interevent displacement at CALS coincides with VT seismicity, we favor the interpretation that vertical displacement per event is closer to 2.5 m, but with only one site on the downdropped block we cannot rule out up to 5 m of collapse.

Our calculations have not accounted for the lava lake conduit, or topographic effects of the preexisting (1500 CE) caldera or newly formed collapse pit as it was expressed in mid-June 2018 at the start of the data analyzed here. Forward models including a conical “pit” with radius 700 m and depth up to 300 m did not significantly alter the conclusions presented here. The pit has greatest effect on horizontal displacements, particularly with the reverse ring fault geometry. Deeper pits and significant disk-shaped calderas have more significant effects. Full three-dimensional modeling with accurate surface topography is beyond our scope but appears unlikely to fundamentally alter our conclusions.

The results above fix the magma chamber geometry to the median values determined from analysis of precollapse deflation. To explore the effects of uncertainty in chamber geometry on inferred properties, we resample from the posterior distribution of Anderson et al. (2019). For a vertical ring fault the surface deformation outside the collapse is simply rigid body translation of the piston plus pressurization of the chamber (Segall et al., 2019) (see also below). Thus, we can employ the model emulator developed by Anderson et al. (2019) to predict the surface deformation due to a co-collapse pressure increase. Least squares estimation of pressure change  $\Delta p_{co}$  given by Equation 2, assuming 2.5 m subsidence per event, along with other parameters, is shown in the SI (Figure S2).  $\Delta p_{co}$  is normally distributed with a mean of 3 MPa and standard deviation of 0.3 MPa. The inferred magma compressibility ranges from roughly  $3 \times 10^{-10}$  to  $2 \times 10^{-9} \text{ Pa}^{-1}$ . While this range is for vertical ring faults, it may reasonably approximate normal faults that steepen to vertical at shallow depth.

Volcano deformation studies often model magma chambers with point source approximations (Lisowski, 2007). To contrast this with the finite source model above, we invert the co-collapse displacements for a triaxial point source. A single point source necessarily combines the contributions of the ring fault and the magma chamber in a single source, although the true source is distributed in depth. We follow the procedure of Davis (1986) and Segall (2010, Chapter 7), using Green’s tensors for a homogeneous half-space, but do not associate the double forces in terms of a pressure boundary condition on a spheroidal magma chamber. We restrict one double force to vertical; relaxing this improves the fit somewhat but does not alter the interpretation. We estimate the source location and the best fitting moment tensor with a Markov chain Monte Carlo (MCMC) procedure.

The point source model fits the data quite well (Figure 5). Posterior distributions for the point source parameters are given in the SI (Figure S3). The median source depth is  $\sim 700$  m, much shallower than the

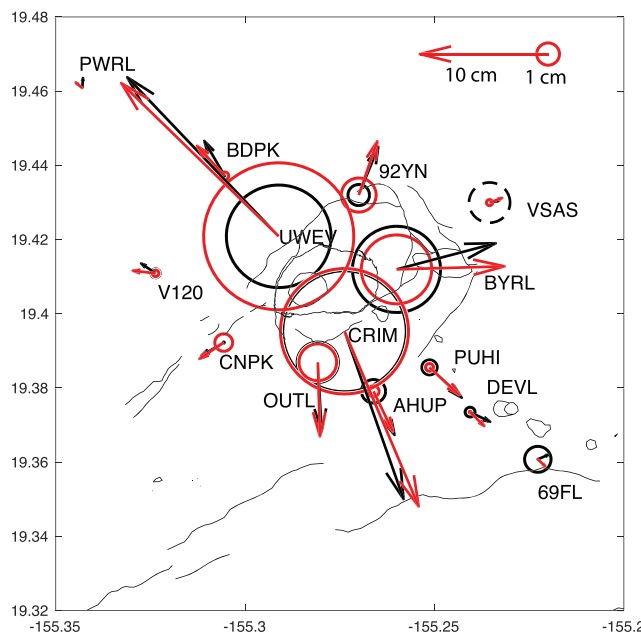


**Figure 5.** Comparison of observed co-collapse displacements (black) with those predicted by a generalized point source moment tensor in an elastic half-space (red). Circles represent vertical displacements, dashed where negative. 10 cm scale for vectors and 1 cm for vertical displacement.

chamber centroid inferred from precollapse data (Anderson et al., 2019). While the point source combines contributions from the ring fault and magma chamber, which are at different depths, it should be dominated by the chamber for near vertical ring faults. Thus, the source depth is unrealistically shallow. The best fitting source is largely isotropic expansion (SI Figure S4a) with minor Compensated Linear Vector Dipole (CLVD) and double-couple components. The vertical double force is maximum; the largest horizontal double force is directed NW/SE reflecting the displacements at UWEV and CRIM (SI Figure S4b) compared to the orthogonal NE/SW direction.

An expansion source might seem counterintuitive for a collapsing caldera, because the “inflationary” deformation observed outside the collapse structure is caused by a volume *decrease* but a pressure *increase*. Consider the case of a vertical ring fault: Due to linearity in the problem, the forward model can be decomposed into (1) displacement of the piston into a magma chamber at constant pressure and (2) the pressurization of the chamber due to the resulting volume decrease. The first step is a rigid body motion and produces no deformation outside the piston. Thus, for a vertical ring fault the pressure increase is the sole cause of deformation external to the caldera. This indicates that there should be some caution in interpreting moment tensor estimates for volumetric sources in terms of source kinematics. We also explored forcing the point source to be located at the *a priori* chamber centroid depth. Not surprisingly, fit to the co-collapse displacements is degraded; in particular, the vertical displacements are significantly overpredicted (SI Figure S5).

As noted above, the collapse faults are normal at the surface, while the geodetic data are consistent with dips steepening with depth. In contrast, many analog and numerical models (Acocella, 2007; Geyer & Martí, 2014; Holohan et al., 2011; Ruch et al., 2012) find initial development of an inner reverse ring fault with subsequent growth of a peripheral fault that may have a normal geometry. In contrast to these studies, the Kilauea collapse was clearly influenced by the presence of the lava lake, Halema‘uma‘u crater, and preexisting caldera bounding structures. In particular, the presence of the lava lake conduit seems to have promoted inward slumping. Another factor favoring normal faulting is regional extension (Acocella, 2007), which is present at Kilauea due to seaward motion of the volcano’s south flank (Denlinger & Morgan, 2014; Owen et al., 2000).

## 5. Conclusions

- Collapse events were accompanied by remarkable “inflationary” deformation external to the caldera with radial outward displacements of nearly 20 cm and uplift of over 5 cm.
- For a constant fault dip the data are best fit by a steeply dipping ( $85^\circ$ ) normal ring fault with a magma estimated to have on the order of 3% bubble volume fraction.
- For lower bubble volume fractions, fit to the stations closest to the caldera is improved if the fault dip increases from roughly  $85^\circ$  to vertical at a depth of  $\sim 600$  m, qualitatively consistent with normal faulting observed at the surface.
- Estimates of pressure increases during collapse events range from 1 to over 3 MPa, depending on magma compressibility. Uncertainty in magma chamber volume alone introduces an uncertainty in pressure change on the order of 0.3 MPa.
- A generalized triaxial point source can fit the data quite well but yields a strongly biased estimate of the source depth and kinematics.

## Data Availability Statement

GPS data are available from the UNAVCO archive (<https://www.unavco.org/data/data.html>).

## Acknowledgments

Thanks to Gary Mavko for discussion, Magnús T. Gudmundsson, J. Gottsmann and Emily Montgomery-Brown for helpful reviews. Any use of trade, firm, or product names is for descriptive purposes only and does not imply endorsement by the U.S. Government.

## References

- Acocella, V. (2007). Understanding caldera structure and development: An overview of analogue models compared to natural calderas. *Earth-Science Reviews*, 85(3-4), 125–160.
- Anderson, K. R., Johanson, I. A., Patrick, M. R., Gu, M., Segall, P., Poland, M. P., et al. (2019). Magma reservoir failure and the onset of caldera collapse at Kilauea volcano in 2018. *Science*, 366(6470), eaaz1822.
- Branney, A., & Acocella, V. (2015). Calderas. In H. Sigurdsson (Ed.), *The encyclopedia of volcanoes* (pp. 299–315). Amsterdam, Boston, Heidelberg: Elsevier.
- Cole, J., Milner, D., & Spinks, K. (2005). Calderas and caldera structures: A review. *Earth-Science Reviews*, 69(1-2), 1–26.
- Davis, P. M. (1986). Surface deformation due to inflation of an arbitrarily oriented triaxial ellipsoidal cavity in an elastic half-space, with reference to Kilauea volcano, Hawaii. *Journal of Geophysical Research*, 91(B7), 7429–7438.
- Denlinger, R. P., & Morgan, J. K. (2014). Instability of Hawaiian volcanoes. *Characteristics of Hawaiian volcanoes U.S. Geological Survey Professional Paper 1801*, 149–176.
- Geyer, A., & Martí, J. (2014). A short review of our current understanding of the development of ring faults during collapse caldera formation. *Frontiers in Earth Science*, 2, 22.
- Gudmundsson, M. T., Jónsdóttir, K., Hooper, A., Holohan, E. P., Halldórsson, S. A., Ófeigsson, B. G., et al. (2016). Gradual caldera collapse at Bárðarbunga volcano, Iceland, regulated by lateral magma outflow. *Science*, 353, 6296.
- Holohan, E., Schöpfer, M., & Walsh, J. (2011). Mechanical and geometric controls on the structural evolution of pit crater and caldera subsidence. *Journal of Geophysical Research*, 116, B07202. <https://doi.org/10.1029/2010JB008032>
- Kumagai, H., Ohminato, T., Nakano, M., Ooi, M., Kubo, A., Inoue, H., & Oikawa, J. (2001). Very-long-period seismic signals and caldera formation at Miyake island, Japan. *Science*, 293(5530), 687–690.
- Lisowski, M. (2007). Analytical volcano deformation source models. In *Volcano deformation* (pp. 279–304). Berlin, Heidelberg, New York: Springer.
- Mavko, G., Mukerji, T., & Dvorkin, J. (2020). *The rock physics handbook*. Cambridge: Cambridge University Press.
- Michon, L., Villeneuve, N., Catry, T., & Merle, O. (2009). How summit calderas collapse on basaltic volcanoes: New insights from the April 2007 caldera collapse of Piton de la Fournaise volcano. *Journal of Volcanology and Geothermal Research*, 184(1-2), 138–151.
- Murase, T., & McBirney, A. R. (1973). Properties of some common igneous rocks and their melts at high temperatures. *Geological Society of America Bulletin*, 84(11), 3563–3592.
- Neal, C., Brantley, S., Antolik, L., Babb, J., Burgess, M., Calles, K., et al. (2019). The 2018 rift eruption and summit collapse of Kilauea volcano. *Science*, 363(6425), 367–374.
- Owen, S., Segall, P., Lisowski, M., Miklius, A., Denlinger, R., & Sako, M. (2000). Rapid deformation of Kilauea volcano: Global Positioning System measurements between 1990 and 1996. *Journal of Geophysical Research*, 105(B8), 18,983–18,998.
- Patrick, M., Dietterich, H., Lyons, J., Diefenbach, A., Parcheta, C., Anderson, K., et al. (2019). Cyclic lava effusion during the 2018 eruption of Kilauea volcano. *Science*, 366(6470), eaay9070.
- Ruch, J., Acocella, V., Geshi, N., Nobile, A., & Corbi, F. (2012). Kinematic analysis of vertical collapse on volcanoes using experimental models time series. *Journal of Geophysical Research*, 117, B07301. <https://doi.org/10.1029/2012JB009229>
- Segall, P. (2010). *Earthquake and volcano deformation*. Princeton and Oxford: Princeton University Press.
- Segall, P., Anderson, K. R., Johanson, I., & Miklius, A. (2019). Mechanics of inflationary deformation during caldera collapse: Evidence from the 2018 Kilauea eruption. *Geophysical Research Letters*, 46, 11,782–11,789. <https://doi.org/10.1029/2019GL084689>
- Shelly, D. R., & Thelen, W. A. (2019). Anatomy of a caldera collapse: Kilauea 2018 summit seismicity sequence in high resolution. *Geophysical Research Letters*, 46, 14,395–14,403. <https://doi.org/10.1029/2019GL085636>
- Spera, F. (2000). Physical properties of magma. In H. Sigurdsson (Ed.), *Encyclopedia of volcanoes* (pp. 171–190). San Diego, Calif. USA: Academic Press.
- Tepp, G., Hotovec-Ellis, A., Shiro, B., Johanson, I., Thelen, W., & Haney, M. M. (2020). Seismic and geodetic progression of the 2018 summit caldera collapse of Kilauea volcano. *Earth and Planetary Science Letters*, 540, 116,250.